

Simulation of the spreading of a gas-propelled micro-droplet upon impact on a dry surface using a lattice-Boltzmann approach

Mahsa Ebrahim,¹ Alfonso Ortega,¹ Nicolas Delbosc,² Mark C. T. Wilson,² and Jonathan L. Summers²

¹Laboratory for Advanced Thermal and Fluid Systems, Villanova University, Villanova, Pennsylvania 19085, USA

²Institute of Thermo-fluids, School of Mechanical Engineering, University of Leeds, Leeds LS2 9JT, United Kingdom

(Received 23 January 2017; accepted 9 June 2017; published online 11 July 2017)

Spray cooling is one of the most promising methods of cooling high heat flux electronics. Depending on the type of the nozzle, spray cooling can be categorized as single-phase or two-phase. In the latter, which is known to be more effective, a secondary gas is used to further pressurize the liquid and form smaller droplets at higher velocities. The gas is also assumed to assist the spreading phase by imposing normal and tangential forces on the droplet free surface which adds to the complicated hydrodynamics of the droplet impact. Moreover, the order of magnitude of droplet size in spray cooling is 10^{-6} m, thereby introducing a low Weber and Reynolds numbers' impact regime which heretofore has not been well understood. A 3D lattice Boltzmann method was implemented to simulate the impact of a single micro-droplet on a dry surface both in ambient air and under a stagnation gas flow. Two cases were closely compared and correlations were proposed for the instantaneous spreading diameter. Contrary to recent findings at higher impact Weber and Reynolds numbers, it was found that a stagnation flow only significantly affects the spreading phase for $Ca^* \geq 0.35$ but has little influence on the receding physics. *Published by AIP Publishing.* [<http://dx.doi.org/10.1063/1.4989546>]

INTRODUCTION

Droplet impingement on solid and liquid surfaces has been extensively investigated due to the numerous applications in ink-jet printing, paint coating, plasma spraying, metal forming, internal combustion engines, microfabrication, and spray cooling of high heat flux surfaces. In the latter application, understanding the fundamental hydrodynamics is of utmost importance in order to avoid dry out or excessive liquid accumulation. Vapor-assisted spray cooling, in which liquid droplets are atomized with a secondary pressurized gas phase, has more complicated physics and has not yet been fully investigated and understood. This technique is known to have a higher heat transfer coefficient,^{1,2} since smaller droplets at higher velocities are formed and impact the surface under a stagnation jet flow. The gas jet flow is also assumed to thin the liquid film by imposing shear stress forces. The current investigation of which this work is a part is designed to experimentally and computationally investigate the basic physics of droplet impingement under the influence of a propellant gas. This paper presents the results of a lattice-Boltzmann numerical study that has allowed the exploration of physics at micro-scale droplet diameters that are common in industrial spray systems. Extension of the regime of investigation to micro-scaled droplets augments the previous investigations by the author's team^{3,4} for meso-scale droplets.

Considerable experimental work has been carried out to investigate the hydrodynamics of the impact of a liquid millimeter-size droplet on a dry solid surface.⁵⁻¹¹ Many

parameters were found to affect the dynamics of the impact, including impact velocity, liquid properties (density, viscosity, surface tension, and Newtonian or non-Newtonian rheology), surface roughness and wettability, droplet size, angle of the impact, surrounding pressure, and surface temperature. Depending on the impact condition, different outcomes can result such as fine deposition, spreading splash, receding break up, or bounce back.¹² It has been observed that maximum spreading is augmented as impact velocity increases.⁷⁻⁹ Viscous droplets are found to spread less, and a noticeably slower receding phase was detected for non-Newtonian droplets.^{8,9,11} It is known that larger droplets and high surface roughness increase the possibility of splashing,^{5,6} while lower surrounding pressure suppresses the droplet disintegration for the same impact conditions.¹⁰ A review of the rich literature of droplet impact on a dry solid surface can be found in Ref. 13.

For practical reasons, most of the investigations in the literature are performed on millimeter-size droplets, whereas in spray cooling, droplet sizes are three orders of magnitude smaller.^{14,15} These micrometer size droplets result in an impact regime of low Weber (We) number and low Reynolds (Re) number regardless of the magnitude of the impact velocity. Son *et al.*¹⁶ experimentally studied the impact of inkjet droplets at low We and Re numbers. They found that the impact dynamics for low We numbers were different from the moderate to high We numbers. Droplet impingement under a stagnation jet flow, which occurs in the gas-assisted spray cooling technique, has undergone little investigation and is not fully understood. The interaction between the

stagnation jet and droplet surface and including especially the influence of the jet normal and shear forces on the hydrodynamics of the impact add to the complexity of the problem. An experimental and numerical investigation on the impact of a gas-propelled millimeter-size water droplet on a heated surface was performed by Diaz and Ortega.^{4,17} Enhancement was observed in the maximum spreading factor of sub-millimeter droplets due to the stagnation pressure on the droplet surface for $We_{gas}/We_{drop} > 0.1$. Ebrahim and Ortega³ investigated gas-propelled droplet impact at considerably higher We numbers ($300 \geq We_{drop} \geq 6000$) and found that while the propellant gas does not enhance spreading, it does retard both the receding and onset of splash.

In the present work, a 3D lattice Boltzmann simulation is developed to study the impact of a micro-sized droplet in the low We and Re numbers' impact regime ($We < 45$, $Re < 450$). The simulation is validated with the experimental data of Briones *et al.*¹⁸ The impact of micro-sized droplets in free-fall in ambient air and under a stagnation air flow is modeled in order to study the hydrodynamics of unassisted and gas-assisted droplet impact, respectively, at these very low droplet diameters.

LATTICE BOLTZMANN METHOD (LBM)

Recently, the lattice Boltzmann method (LBM) has shown to be a powerful method for the numerical simulation of complex flows such as porous media flows and multiphase flows. The LBM is a mesoscopic method that covers the gap between the microscopic molecular dynamics and the macroscopic fluid mechanics. The mesoscopic nature of LBM yields a practical way of implementing microscopic dynamics between fluid-fluid and fluid-solid interactions as it solves the discrete form of the Boltzmann equation in the bulk flow.¹⁹ In the LBM, the fluid field consists of similar particles that are allowed to move in specific directions, and the flow motion is captured by a set of distribution functions. The studies of LBM are numerous, and therefore here we only review and discuss the multiphase LBM suitable for current investigations.

Different methods for multiphase LBM simulations have been developed and can be categorized as chromodynamic (Gunstensen *et al.*²⁰), free energy (Swift *et al.*²¹), pseudo-potential (Shan and Chen²²), and finite density (He *et al.*²³). The Shan and Chen model is the most popular multiphase LB model because of its simplicity and computational efficiency. A complete review of the pseudo-potential models can be found in the work of Chen *et al.*²⁴ The advantages of the model of He *et al.* are its thermodynamic consistency and the ability to vary densities and viscosities independently. Its use is restricted to nearly incompressible single-component flows with two phases.

In the present work, the method of He *et al.*²³ is implemented to simulate the impact of a free-falling droplet in ambient air and the impact of a droplet under a stagnation air jet flow. This method is briefly explained in the section titled Method of He *et al.* Further details of this method can be found in Ref. 23.

Method of He *et al.*

Using the Bhatnagar-Gross-Krook single relaxation time approximation, the general Boltzmann equation for non-ideal fluids can be written as²⁵

$$\frac{\partial f}{\partial t} + \mathbf{e} \cdot \nabla f = -\frac{f - f^{eq}}{\tau} + \frac{(\mathbf{e} - \mathbf{v}) \cdot (\mathbf{F} + \mathbf{G})}{\rho RT} f^{eq}, \quad (1)$$

where \mathbf{F} is the effective molecular interaction, \mathbf{G} is the gravity force, R is the gas constant, T is the temperature, \mathbf{e} and \mathbf{v} are the microscopic (i.e., molecular) and macroscopic velocities, respectively, ρ is the macroscopic fluid density, and $f(\mathbf{x}, \mathbf{e}, t)$ is the single-particle probability distribution function, with local equilibrium value given by

$$f^{eq}(\mathbf{v}) = \frac{\rho}{(2\pi RT)^{\frac{3}{2}}} \exp\left(\frac{-(\mathbf{e} - \mathbf{v})^2}{2RT}\right). \quad (2)$$

The effective molecular interaction force can be defined based on the mean-field approximation²³ as follows:

$$\mathbf{F} = -\nabla \psi + \mathbf{F}_s, \quad (3)$$

where the first term on the right hand side of Eq. (3) represents the interaction due to the non-ideal part of the equation of state (EOS) and the second term is associated with the surface tension force, which is given as follows:

$$\psi(\rho) = P - \rho RT, \quad \mathbf{F}_s = \kappa \rho \nabla \nabla^2 \rho, \quad (4)$$

where κ determines the strength of surface tension force and in this work pressure, P , is obtained from the Carnahan and Starling EOS.²⁶ Since the evolution of $\nabla \psi$ across the interface is large, and hence evaluation of the inter molecular force can lead to instability, He *et al.*²³ introduced an auxiliary pressure distribution function given by

$$g = fRT + \psi(\rho)\Gamma(0), \quad (5)$$

where

$$\Gamma(\mathbf{v}) = \frac{f^{eq}(\mathbf{v})}{\rho}. \quad (6)$$

The macroscopic pressure and velocity can then be obtained by integrating the g distribution function as follows:

$$P = \int g d\mathbf{e}, \quad \rho RT \mathbf{u} = \int \mathbf{e} g d\mathbf{e}. \quad (7)$$

He *et al.*²³ proposed a mass index function of $\phi = \int f d\mathbf{e}$, where f is obtained from Eq. (1). The role of ϕ is to keep track of the two separate phases and hence the shape and position of the interface between them. The densities and viscosities of the phases of interest are mapped onto ϕ and are determined by a simple interpolation of the index function, given by

$$\rho = \rho_g + \frac{\phi - \phi_g}{\phi_l - \phi_g} (\rho_l - \rho_g), \quad \nu = \nu_g + \frac{\phi - \phi_g}{\phi_l - \phi_g} (\nu_l - \nu_g), \quad (8)$$

where ρ_l and ρ_g are liquid and vapor densities, respectively. Similarly, ν_l and ν_g stand for the liquid and vapor viscosities, and ϕ_l and ϕ_g are the minimum and maximum values of the index function.²³

To proceed with a numerical scheme, the above equations must be discretized to produce the corresponding lattice

Boltzmann equations. This involves discretizing the microscopic velocity space into a set of discrete velocities, \mathbf{e}_i , and evaluating the moment integrals, Eq. (7), by quadrature.^{19,23} This discretization of velocity is linked to the discretization of space by defining a lattice where the spacing between neighboring nodes is given by $\mathbf{e}_i\delta t$, where δt is the time step. In this study, the standard D3Q19 lattice is used, in which each node has links to its 18 nearest neighbors.

Following the analysis of He *et al.*,²³ final discrete forms of the evolution equations with the change of variables of $\bar{f}_i = f_i + \tilde{\mathbf{F}}_i$ and $\bar{g}_i = g_i + \tilde{\mathbf{G}}_i$ (to create an explicit scheme) are given as

$$\bar{f}_i(\mathbf{x} + \mathbf{e}_i\delta t, \mathbf{e}_i\delta t) - \bar{f}_i(\mathbf{x}, \delta t) = -\frac{1}{\tau}(\bar{f}_i(\mathbf{x}, \delta t) - f_i^{eq}(\mathbf{x}, \delta t)) - \frac{2\tau - 1}{\tau}\tilde{\mathbf{F}}_i, \quad (9)$$

$$\bar{g}_i(\mathbf{x} + \mathbf{e}_i\delta t, \mathbf{e}_i\delta t) - \bar{g}_i(\mathbf{x}, \delta t) = -\frac{1}{\tau}(\bar{g}_i(\mathbf{x}, \delta t) - g_i^{eq}(\mathbf{x}, \delta t)) - \frac{2\tau - 1}{\tau}\tilde{\mathbf{G}}_i, \quad (10)$$

where

$$\tilde{\mathbf{F}}_i = \frac{\delta t}{2RT}(\mathbf{e}_i - \mathbf{v}) \nabla \psi(\phi)\Gamma_i(\mathbf{v}), \quad (11)$$

$$\tilde{\mathbf{G}}_i = -\frac{\delta t}{2}(\mathbf{e}_i - \mathbf{v})[\Gamma_i(\mathbf{v})(\mathbf{F}_s + \mathbf{G}) - (\Gamma_i(\mathbf{v}) - \Gamma_i(0)) \cdot \nabla \psi(\rho)], \quad (12)$$

and

$$\Gamma_i(\mathbf{v}) = \omega_i \left(1 + \frac{3}{c^2}(\mathbf{e}_i \cdot \mathbf{v}) + \frac{9}{2c^4}(\mathbf{e}_i \cdot \mathbf{v})^2 - \frac{3}{2c^2}\mathbf{v}^2 \right), \quad (13)$$

where $c = \sqrt{3RT}$ and ω_i are weights arising from the quadrature. The corresponding discrete equilibrium distribution functions are given by $f_i^{eq}(\mathbf{v}) = \rho\Gamma_i(\mathbf{v})$ and $g_i^{eq}(\mathbf{v}) = \rho RT\Gamma_i(\mathbf{v}) + \psi(\rho)\Gamma_i(0)$.

The macroscopic variables can be computed from

$$\phi = \sum_i \bar{f}_i, \quad (14)$$

$$P = \sum_i \bar{g}_i - \frac{1}{2}\mathbf{v} \cdot \nabla \psi(\rho)\delta t, \quad (15)$$

$$\rho RT\mathbf{u} = \sum_i \mathbf{e}_i \bar{g}_i + \frac{RT}{2}(\mathbf{F}_s + \mathbf{G})\delta t, \quad (16)$$

where ρ is obtained by interpolating the index function through Eq. (8) and $\psi(\phi)$ is computed from Eq. (4) using the Carnahan and Starling EOS, where $b = 4$,

$$\psi(\phi) = P - \frac{\phi}{3} = \phi^2 \left(\frac{2RT(2 - \phi)}{(1 - \phi)^3} - 4 \right). \quad (17)$$

It should be noted that the choice of a in the EOS affects ϕ_l and ϕ_g through the coexistence curve and Maxwell's equal area rule. $\psi(\rho)$ is calculated using the numerically obtained P from the simulation. Since fluid kinetic viscosity is coupled with the relaxation time [$\nu = c_s^2\delta t(\tau - \frac{1}{2})$] and the index function [Eq. (8)], the relaxation time varies across the interface. Moreover, a six-point stencil finite difference approach with a second order accuracy is used to calculate the gradient of $\psi(\rho)$.

The wettability of wall

To model the fluid-solid interaction (wall wettability) in the work of He *et al.*,²³ Davies *et al.*²⁷ proposed a wetting boundary condition by applying the surface affinity concept²⁸ to the index function. The surface affinity, χ , is defined as

$$\chi = \frac{\phi - \frac{1}{2}(\phi_l + \phi_g)}{\phi_l - \phi_g} \quad (18)$$

such that $\chi = -1$ and $\chi = +1$ represent hydrophobic and hydrophilic surfaces, respectively. Iwahara *et al.*²⁸ related the equilibrium contact angle to the surface affinity through Young's equation as follows:

$$\cos(\theta_{eq}) = \frac{\chi}{2}(3 - \chi^2). \quad (19)$$

Therefore, the equilibrium contact angle, which is related to the wettability of the solid surface, specifies the wall surface affinity. Then, this value of surface affinity prescribes the index function of the wall (ϕ_s) that affects $\psi(\phi)$ via Eq. (17). The gradient of $\psi(\phi)$ at the solid wall can be numerically calculated using a non-equilibrium bounce back boundary condition at the wall. This gradient is finally used in the force terms [Eqs. (11) and (12)] of the lattice Boltzmann equations. Further details of the wetting boundary condition can be found in Ref. 27.

RESULTS AND DISCUSSION

Three-dimensional micro-meter size water droplets were simulated for a density ratio of $\rho_l/\rho_g = 10$ and interface thickness of 1.5. Note that this density ratio is substantially lower than the water/air ratio of the experiments used for validation. As with many diffuse interface/LB models, setting the density ratio too high leads to numerical instability and simulation failure. Here, a value is chosen at the upper end of the stable range for this model, where predictions are found to become insensitive to the specific value of the density ratio. In the first set of results, the droplet impingement in free-fall in ambient air was investigated for different impact conditions. In the second set, the impingement under a stagnation air flow was modeled and the two cases were compared.

Droplet impact in free-fall in ambient air

The simulations were initialized with a droplet positioned in the center of the domain with a downward velocity of V_0 . Periodic boundary conditions were set for the side boundaries, and wetting wall boundary conditions were set for the top and bottom boundaries. The schematic of the problem domain and boundary conditions is shown in Fig. 1.

The range of the parameters varied in the simulations is listed in Table I, including the Weber number (We), Reynolds number (Re), Ohnesorge number (Oh), capillary number (Ca), droplet initial diameter (D_0), droplet impact velocity (V_0), and equilibrium contact angle (θ_{eq}). The We, Re, Oh, and Ca numbers are defined as

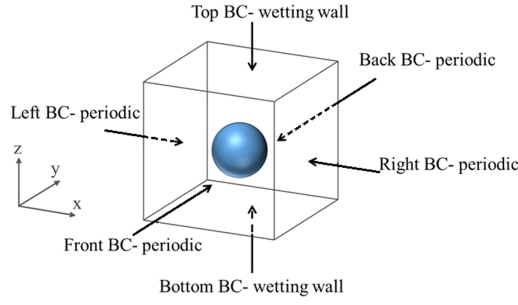


FIG. 1. Schematic of the problem domain and boundary conditions.

$$\text{Re} = \frac{\rho V_0 D_0}{\mu}, \quad \text{We} = \frac{\rho V_0^2 D_0}{\sigma}, \quad (20)$$

$$\text{Oh} = \frac{\sqrt{\text{We}}}{\text{Re}} = \frac{\mu}{\sqrt{\rho \sigma D_0}}, \quad \text{Ca} = \frac{\text{We}}{\text{Re}} = \frac{\mu V_0}{\sigma}. \quad (21)$$

Validation

The experimental data of Briones *et al.*¹⁸ were used to validate the three-dimensional LBM simulation of this study. Operating conditions for each impact case are listed in Table II and were exactly matched in each simulation. The maximum spreading factor, $\xi_{\max} = D_{\max}/D_0$, of the LBM simulation is compared to the experimental data in Fig. 2 with respect to the dimensionless time $\tau = tV_0/D_0$. It can be seen that the simulation results agree well with the experiments to within $\pm 5.5\%$ error. The instantaneous dimensionless droplet diameter during the spreading phase, $\xi = D/D_0$, for the two impact cases B and D is illustrated in Fig. 3. Good agreement is observed for $\tau > 0.4$. For very early times, $\tau < 0.2$, the LBM simulations strongly under-predict the data. The good agreement at later times and the ability to predict the maximum spreading diameter indicate that the LBM approach can reveal droplet impact physics with a good degree of confidence during the majority of the spreading regime.

Spreading regime in free fall

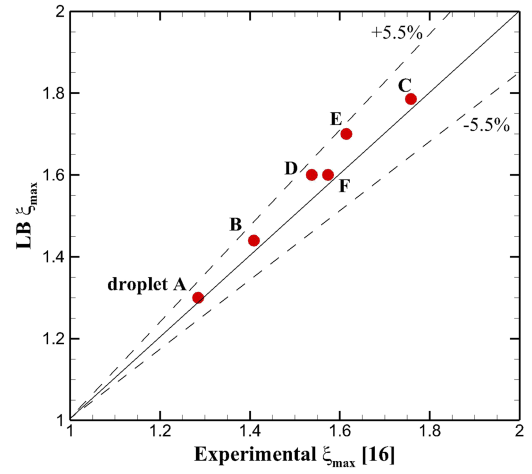
As pointed out by Ebrahim and Ortega,³ immediately after impact, the droplet experiences a collapsing regime, in

TABLE I. Variation of different parameters in the simulations.

	We	Re	Oh $\times 10^3$	Ca	D_0 (μm)	V_0 (m/s)	θ_{eq} (deg)
min	1.4	40	8.3	0.035	2.7	1.2	30
max	42	410	70.7	0.102	200	11	98

TABLE II. Operating conditions of the experimental data.¹⁸

Droplet	D_0 (μm)	V_0 (m/s)	We	Re	Oh $\times 10^3$	θ_{eq} (deg)
A	40.7	1.56	1.4	63.4	26	87.09
B	35.6	3.02	4.5	107.3	28	79.04
C	55.4	2.45	4.6	135.5	22	50.32
D	36.6	4.02	8.2	146.8	28	65.66
E	32.2	5.14	11.8	165.2	29	64.45
F	33.4	4.97	11.4	165.7	29	66.69

FIG. 2. Maximum spreading factor of LBM simulation vs. experimental data.¹⁸

which a spherical droplet begins to deform to a lamella with a defined contact line. For moderate to high impact conditions, this regime has a very short duration and therefore is usually neglected. After the formation of the lamella, the spreading phase continues until the droplet initial kinetic energy is completely converted to surface tension energy of the stretched lamella and dissipated by the wall shear stress. After the droplet reaches its maximum spreading diameter, the receding phase is initiated by the surface tension force that induces the retraction of the initially stretched droplet until it achieves a new static equilibrium state. Depending on the surface wettability and temperature, the droplet may continue to recede until it rebounds completely or partially from the surface. The equilibrium state is eventually achieved after experiencing a number of oscillations between the spreading and receding phases. This paper focuses only on the spreading phase. The continuing study is focusing on the receding phase. Figure 4 illustrates the time elapsed images of the simulations during the spreading phase for two impact conditions.

Numerous analytic models have been proposed to determine the maximum spreading diameter for the moderate to high impact We and Re numbers.^{29–33} There are however few

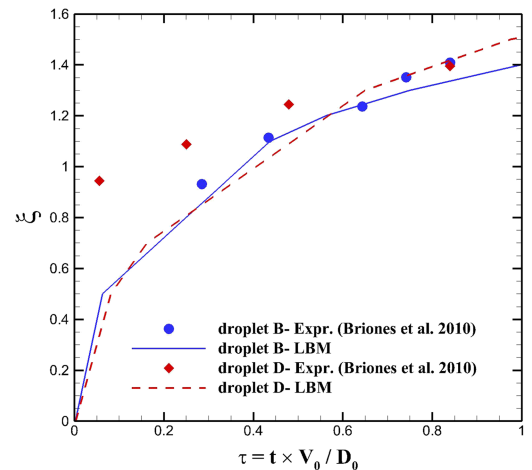


FIG. 3. Instantaneous spreading factor.

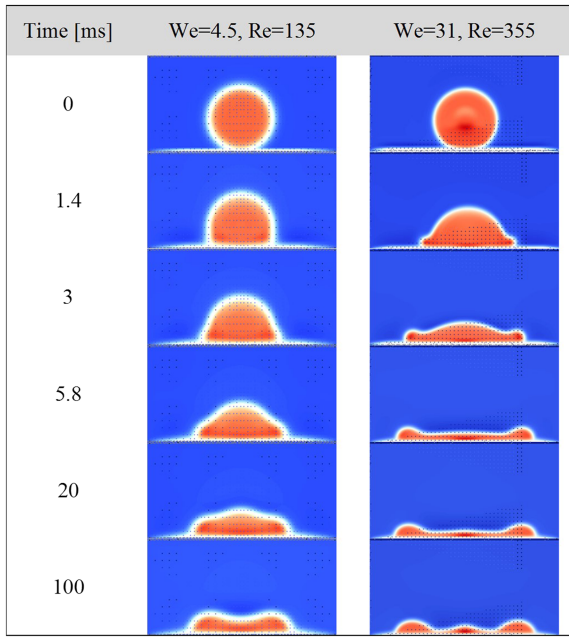


FIG. 4. Time elapsed images of the LBM simulations.

dynamic models to compute the instantaneous droplet diameter.^{34–36} Several of these models are presented in Table III and are compared against the experimental data of Briones *et al.*,¹⁸ Fig. 5 presents the error in predicting the maximum spreading diameter, ξ_{max} , using these models. The correlation of Scheller and Bousfield³⁷ and the model of Son *et al.*¹⁶ are accurate for all case studies ($1 < We < 12$) to within $\pm 25\%$. The models of Attane *et al.*³⁴ and Pasandideh-Fard *et al.*³⁰ are reasonable for $8 < We$. The remaining models fail to adequately predict the behavior of these micro-droplets. One possible reason for the failure of these models is that they are based on the energy balance approach, in which a cylindrical shape droplet is assumed immediately after impact. Son *et al.*¹⁶ speculated that this assumption is not valid for micrometer size droplet impact because no lamella formation was observed in their

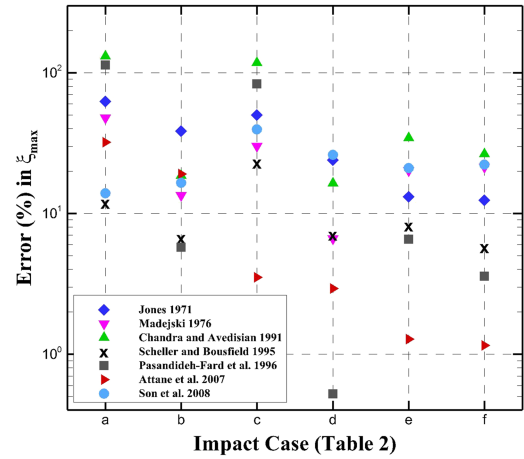


FIG. 5. Comparison of analytical models in Table III with the experimental data of Briones *et al.*,¹⁸ model of Yang³¹ does not have real roots for these case studies.

experiments performed in the low We and Re numbers' impact regime. Those observations are confirmed in Fig. 4, where low and high impact conditions are compared. Therefore, a simple model or correlation to predict the dynamic spreading diameter within the low We and Re numbers impact regime must acknowledge these physics and remains undeveloped until now.

Correlation for spreading phase

In order to propose a correlation for the spreading phase, it is essential to distinguish the correct time and length scales to properly collapse and normalize data. Therefore, the first step is to find and study the major dimensionless groups and parameters that individually affect the spreading dynamics. As previously mentioned, the main dimensionless groups describing the hydrodynamics of the droplet impact are Re, We, Oh, and Ca numbers. Note that Oh and Ca are not independent; the key dimensionless numbers are clearly We and Re. In comparing micro(micrometer)-size and macro(millimeter)-size droplet impingement, it is necessary to match any two

TABLE III. Analytic models to predict maximum spreading diameter.

Model	Equation
Chandra and Avedisian ²⁹	$\frac{3}{2} \frac{We}{Re} \xi_{max}^4 + (1 - \cos\theta) \xi_{max}^2 - \left(\frac{We}{3} + 4\right) = 0$
Yang ³¹	$\frac{We}{2} = \frac{3}{2} \xi_{max}^2 \left(1 + \frac{3We}{Re} \left(\xi_{max}^2 \ln \xi_{max} - \frac{\xi_{max}^2 - 1}{2}\right) \left(\frac{\mu_{drop}}{\mu_{wall}}\right)^{0.14}\right) - 6$
Jones ³²	$\xi_{max} = \left(\frac{We}{6}\right)^{0.5}$
Madejski ³³	$\frac{3\xi_{max}^2}{We} + \frac{1}{Re} \left(\frac{\xi_{max}}{1.2941}\right)^5 = 1$
Pasandideh-Fard <i>et al.</i> ³⁰	$\xi_{max} = \sqrt{\frac{We+12}{3(1-\cos\theta)+4\left(\frac{We}{\sqrt{Re}}\right)}}$
Attane <i>et al.</i> ³⁴	$\frac{1}{2} \frac{d}{dt} \left[\frac{1}{2} + \frac{1}{27} \frac{1}{r^6} \left(\frac{dr}{dt}\right)^2 \right] + \frac{1}{dt} \left[r^2(1 - \cos\theta_{eq}) + \frac{1}{3r} \right] + \frac{\Lambda}{2} Oh r^2 \left(\frac{dr}{dt}\right)^2$
Son <i>et al.</i> ¹⁶	$\xi_{max} = \sqrt{\frac{We+12}{3(f_s - \cos\theta) + 4\left(\frac{We}{\sqrt{Re}}\right)}}, f_s = 1 + \left[1 - \frac{\cos\theta}{\cos(90 - \theta)}\right]^2$
Scheller and Bousfield ³⁷	$\xi_{max} = 0.61(Re^2 Oh)^{0.133}$

of these dimensionless groups. It is possible to match impact We number of micro- and macro-size droplets by varying the impact velocity, but the Re number of a micro-droplet will be at least one order of magnitude smaller than that of the macro-droplet, regardless of the impact velocity. The flow therefore will be dominated by low Re number physics which would tend towards creeping flow rather than collapsing and flattening to a lamella. This is substantiated in the experiments of Son *et al.*¹⁶ and likely contributes to the failure of most of the analytic models.

Surface wettability, which is commonly defined in terms of equilibrium contact angle, can also independently affect impact dynamics. This phenomenon depends on the chemical properties of the surface and the liquid,^{38,39} and therefore the wettability of a pure liquid varies on different surfaces. It should be noted that surface wettability is often confused with surface tension modification. The effect of surface tension modification is captured in the We number.

The individual effects of We and Re numbers obtained from lattice Boltzmann simulations are shown in Figs. 6(a) and 6(b). Droplet diameter and impact velocity are adjusted so as to maintain one dimensionless number constant while varying the other. The separate influences of We and Re numbers illustrate the distinct effects of droplet surface tension and viscosity on the spreading phase. The effect of the We number is illustrated in Fig. 6(a). When the We number is increased, the rate of the spreading phase is not significantly affected because the enhancement in the We number is primarily due to the decrease in surface tension. Therefore, for a given kinetic energy and viscous dissipation, a weakened opposing surface tension force will cause the spreading phase to continue longer without significant change in the rate and lead to a larger spreading diameter. Figure 6(b) demonstrates the significant influence of the Re number on the dynamics of the impact primarily due to the influence of the initial droplet kinetic energy. Rioboo *et al.*⁷ made similar observations for the individual effects of We and Re numbers for millimeter-size droplet impact. The influence of surface wettability is illustrated in Fig. 6(c). It is clear that as the equilibrium contact angle decreases or as the surface becomes more hydrophilic, the rate and the extent of the maximum spreading diameter are enhanced.

Further study of Fig. 6 shows that the dimensionless time, $\tau = t \times \frac{V_0}{D_0}$, fails to normalize the time of the spreading dynamics, except for cases where the Re number is varied. Therefore, a more appropriate time scale to normalize the dynamic time must depend on the We number and surface wettability, which are both incorporated in the surface tension force. Using the surface tension force and the acceleration it causes during the spreading phase, the spreading time scale, t_s , can be approximated as follows:

$$F_{\text{surfaceTension}} \propto M_d \left(\frac{V_0}{t_s} \right), \quad (22)$$

$$\sigma D_0 (1 - \cos \theta) \propto \rho D_0^3 \frac{V_0}{t_s} \rightarrow t_s \propto \left(\frac{\text{We}}{1 - \cos \theta} \right) \frac{D_0}{V_0}, \quad (23)$$

where M_d and V_0 are the mass and initial velocity of the droplet, respectively. The time scale, t_s , was empirically modified based on Eq. (23) to scale the spreading dynamics more accurately as follows:

$$t_s = \left(\frac{\text{We}}{1 - \cos \theta} \right)^{\frac{1}{4}} \frac{D_0}{V_0}. \quad (24)$$

The new dimensionless time for spreading phase, τ^* , is then defined as

$$\tau^* = \frac{t}{t_s} = \tau \left(\frac{1 - \cos \theta}{\text{We}} \right)^{\frac{1}{4}}, \quad (25)$$

where $\tau = tV_0/D_0$ is the common dimensionless time previously used in the literature. It is also clear in Fig. 6 that the non-dimensional length, $\xi = \frac{D}{D_0}$, fails to normalize the spreading diameter. Since the dynamic diameter is affected by both the initial droplet size, D_0 , and impact velocity, V_0 , the maximum spreading diameter would be a more appropriate length scale because it captures the effects of both the initial diameter and velocity. It is also evident from Fig. 6 that the droplet diameter during the spreading phase is more significantly affected by the Re number or viscosity. Hence, the dominant terms in approximating the length scale are viscous dissipation and initial kinetic energy. The new length scale, D_s , can be estimated from the time in which all the initial kinetic energy is dissipated and the droplet reaches its maximum spreading diameter as follows:

$$\frac{1}{2} M_d V_0^2 \propto \mu \left(\frac{dv}{dr} \right)^2 D_0^3 t_s, \quad (26)$$

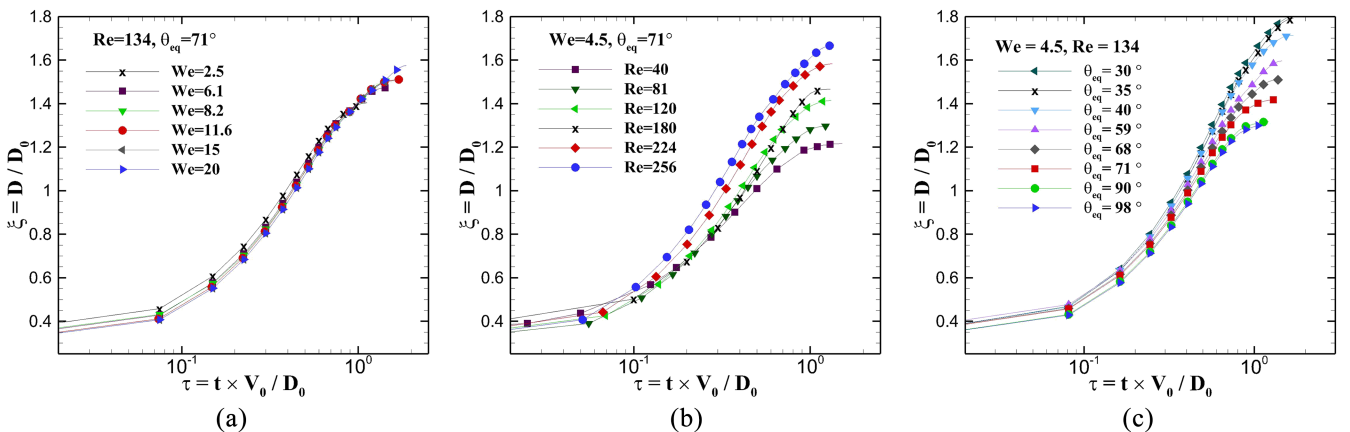


FIG. 6. Instantaneous spreading factor for different impact (a) We numbers, (b) Re numbers, and (c) contact angles.

$$\rho D_0^3 V_0^2 \propto \mu \left(\frac{D_{max}/t_s}{D_0} \right)^2 t_s D_0^3. \quad (27)$$

Introducing Eq. (24) will lead to

$$D_s \propto D_0 \text{Re}^{\frac{1}{2}} \left(\frac{\text{We}}{1 - \cos \theta} \right)^{\frac{1}{8}}. \quad (28)$$

It was empirically observed that reducing the power of the Re number in Eq. (28) to $\frac{1}{8}$ in order to group the dimensionless numbers together will not significantly affect the normalization results. Therefore, in order to have neater and simpler curve fit results, Eq. (28) was empirically modified to

$$D_s = D_0 \left(\frac{\text{ReWe}}{1 - \cos \theta} \right)^{\frac{1}{8}}. \quad (29)$$

The dimensionless length for the spreading phase will thus be

$$\xi^* = \xi \left(\frac{(1 - \cos \theta)}{\text{WeRe}} \right)^{\frac{1}{8}}. \quad (30)$$

The effectiveness of the introduced dimensionless length, ξ^* , and the dimensionless time, τ^* , is presented in Fig. 7 where the same simulation data of Fig. 6 are normalized using Eqs. (25) and (30). It is clear that the new length and time scales can significantly improve normalizing the impact dynamics. It is also evident that the spreading phase ends at $\tau_{max}^* \approx 0.79$ for all case studies.

The normalized instantaneous spreading phase for numerous impact conditions is illustrated in Fig. 8. A curve fit of the normalized data, given as Eq. (31), is reasonably accurate to predict the instantaneous spreading diameter to within $\pm 16\%$ for low We and Re numbers and for $0.02 \leq \tau^*$. It should be noted that the error is higher for early spreading ($\tau^* \leq 0.02$) because the collapsing process that is usually neglected has different physics and scaling characteristics,

$$\xi^* = (\tau^*)^{\frac{1}{2}} (e^{-0.46\tau^*}) \quad (31)$$

for $2.5 \leq \text{We} \leq 41.8$, $40 \leq \text{Re} \leq 410$, and $0 \leq \tau^* \leq 0.79$. Figure 8 also further confirms that the normalized spreading phase ends at the dimensionless time of $\tau_{max}^* \approx 0.79$ and

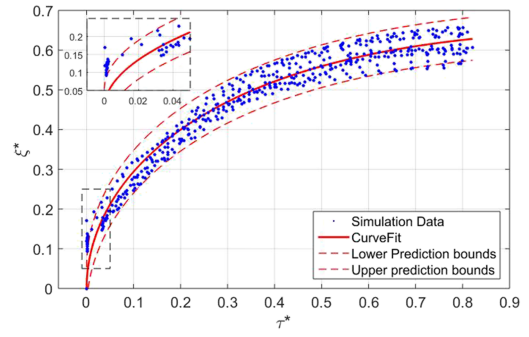


FIG. 8. Normalized instantaneous spreading diameter for free falling droplet in ambient air. Simulation data variation: $2.5 \leq \text{We} \leq 42$, $40 \leq \text{Re} \leq 410$, and $30^\circ \leq \theta_{eq} \leq 98^\circ$.

therefore time to the maximum spreading diameter of any impact condition can be determined as

$$t_{max} = \tau_{max}^* t_s = 0.79 \frac{D_0}{V_0} \left(\frac{\text{We}}{1 - \cos \theta} \right)^{\frac{1}{4}}. \quad (32)$$

Since ξ_{max}^* is gained at $\tau_{max}^* = 0.79$, the maximum spreading factor is given as

$$\xi_{max} = 0.6180 \left(\frac{\text{WeRe}}{1 - \cos \theta_{eq}} \right)^{\frac{1}{8}}. \quad (33)$$

The instantaneous spreading factor can be calculated by substituting Eqs. (30) and (25) in Eq. (31) as follows:

$$\xi = \text{Re}^{\frac{1}{8}} \tau^{\frac{1}{2}} \exp \left(-0.46\tau \left(\frac{1 - \cos \theta}{\text{We}} \right)^{\frac{1}{4}} \right). \quad (34)$$

The error in predicting the maximum spreading diameter using Eq. (33) with respect to the experimental data is shown in Fig. 9 and compared against the previous analytical models that were introduced in Table III. Figure 9 further demonstrates the ability of the proposed correlation to reasonably predict the maximum spreading diameter in low impact regimes. The proposed correlations, Eqs. (33) and (34), can be used to reasonably approximate the instantaneous droplet diameter and the maximum spreading diameter, respectively,

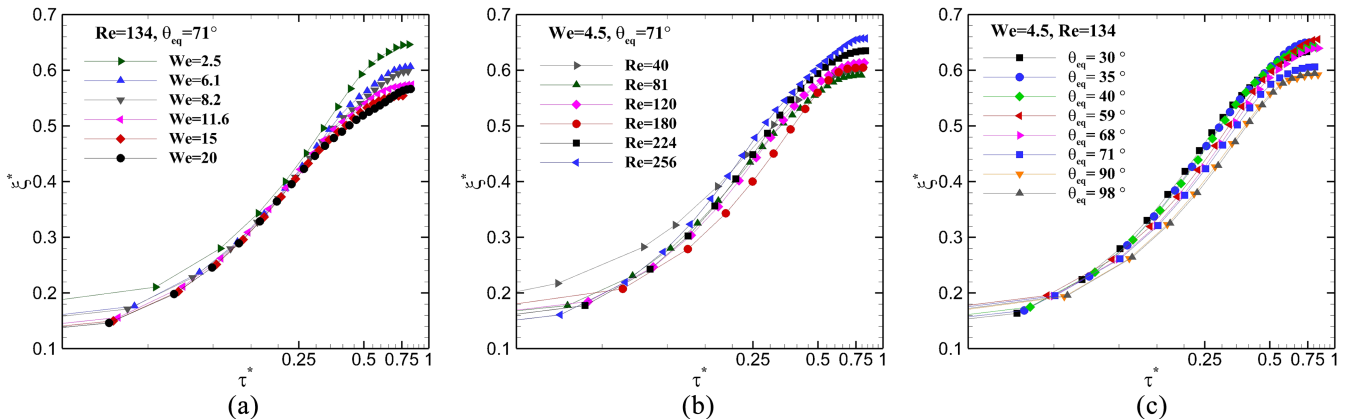


FIG. 7. The effect of new dimensionless length and time in normalizing spreading dynamics for different impact (a) We numbers, (b) Re numbers, and (c) contact angles.

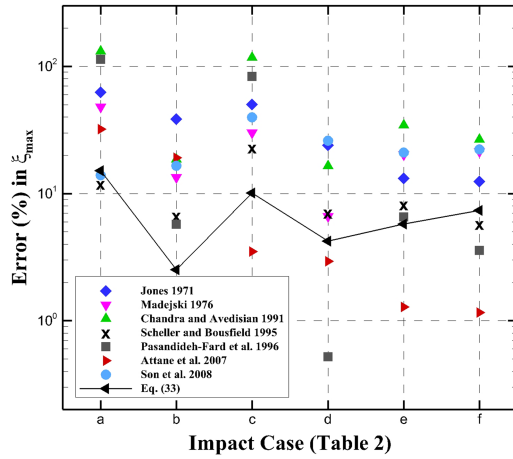


FIG. 9. Comparison of Eq. (33) and analytical models in Table III with the experimental data of Briones *et al.*¹⁸

for a droplet impact within the unassisted spray cooling scale, $10 \leq D \leq 100 \mu\text{m}$ and $1 \leq V_0 \leq 25 \text{ m/s}$.^{14,15,40,41}

Droplet impact under a stagnation air jet

As previously mentioned, vapor-assisted spray cooling is known to be more efficient in heat removal than the regular unassisted spray cooling. In this technique, gas-atomizing nozzles with pressurized gas are used to create smaller droplets with higher velocities in a gas stagnation flow field. The gas is hypothesized to thin the liquid film that is formed after the impact of each droplet by imposing shear stress on the droplet surface. Therefore, the heat transfer is speculated to be enhanced due to the formation of a larger contact area and thinner liquid film on the target surface. However, the effect of the gas jet flow on the dynamics of the droplet impact is not fully understood.

Effect of the stagnation jet flow

In this section, the impact of a water droplet under an air jet flow is simulated and hence a stagnation jet is added to the spreading phase and boundary conditions are changed accordingly. The boundary condition method proposed by Chang *et al.*⁴² and Liu *et al.*⁴³ was applied to change the boundaries into inlet-velocity or pressure-outlet boundary conditions.

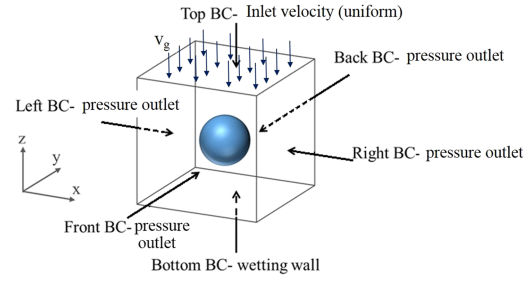


FIG. 10. Schematic of the droplet impact under a stagnation jet flow.

At each boundary, the unknown distribution functions are estimated based on their equilibrium distribution function with an additional correction factor as follows:

$$\bar{f}_i = \bar{f}_i^{eq} + \omega_i Q_f, \quad (35)$$

$$\bar{g}_i = \bar{g}_i^{eq} + \omega_i e_i \cdot Q_g, \quad (36)$$

where Q_f and Q_g are the correction factors for each boundary and can be determined by satisfying the conservation of mass and momentum, respectively. The top boundary was changed to inlet-velocity, where the density and all the velocity components are known and the pressure is unknown. All the side boundaries were modified to the pressure-outlet boundary condition, where the density and pressure are known, velocity components parallel to the boundary are considered zero, and the velocity component perpendicular to the boundary is unknown. Jet-to-surface distance was considered $H/D_0 = 2.5$ and the droplet was initially positioned in the middle of the domain with an initial velocity, V_0 . The effect of the jet on the droplet acceleration was neglected due to the fact that the distance travelled by the droplet before the impact is too short. A schematic of the problem domain and boundary conditions is shown in Fig. 10.

The effect of jet average velocity is demonstrated in Fig. 11 for the droplet impact condition of $Re = 135$, $\theta_{eq} = 71.1^\circ$, and $We = 4.5$ and 14.5 , where the gas We number is defined as $We_g = \rho_g V_g^2 D_0 / \sigma$, where V_g is the jet velocity and ρ_g is the gas density. It can be seen in Fig. 11(a) that the stagnation jet does not significantly affect the maximum spreading diameter for $We_g < 0.09$, while considerable enhancement is observed in both the rate and extent of the spreading for $We_g \geq 0.09$. It should be noted that the gas affects the early spreading phase for $We_g < 0.09$; however, this phase

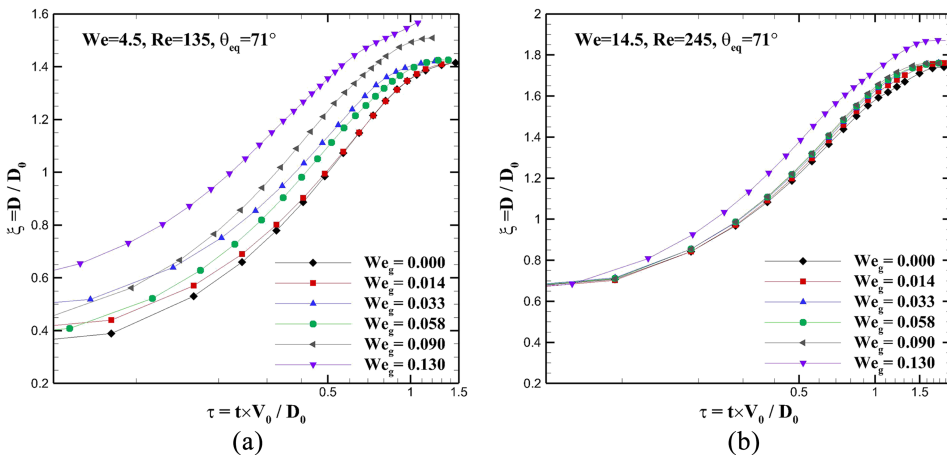


FIG. 11. Instantaneous spreading factor for different We_g for the impact condition of $Re = 245$ and $\theta_{eq} = 71.1^\circ$. (a) $We = 4.5$ and (b) $We = 14.5$.

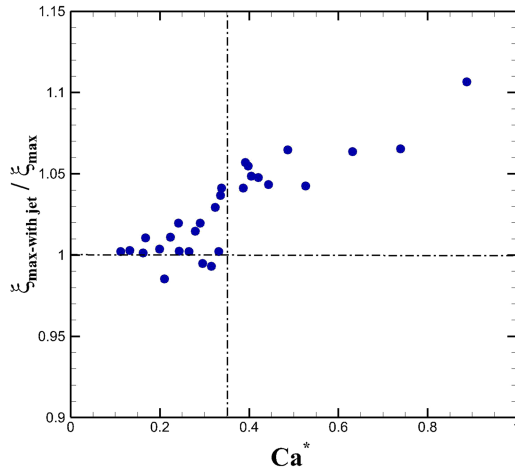


FIG. 12. Ratio of maximum spreading diameter under the stagnation jet flow to maximum spreading diameter in ambient air. Simulation data variation: $2.5 \leq We \leq 42$, $40 \leq Re \leq 410$, and $0.014 \leq We_g \leq 0.23$.

is usually neglected due to its complicated physics and rapid behavior. The same influence can be seen in Fig. 11(b), with the exception that the stagnation jet starts to affect the spreading phase for $We_g \geq 0.13$. It is clear that jet shear stress on the droplet surface increases as We_g is augmented. However, jet normal and tangential forces have to be sufficiently strong compared to the droplet spreading kinetic energy in order to affect and assist the maximum spreading diameter.

It is necessary to determine the critical We_g at which the stagnation jet flow starts to influence the spreading phase and further stretches the maximum spreading diameter. Figure 12 represents the normalized results of various impact conditions. It is evident that for $Ca^* \geq 0.35$, a more significant effect is observed in the maximum spreading diameter $\xi_{max-withjet} / \xi_{max} > 1$, and therefore we define Ca^* as the critical effective point given as

$$Ca^* = \frac{We^*}{Re^*} \geq 0.35, \quad (37)$$

where $We^* = \frac{We_g}{We} = \frac{\rho_g V_g^2}{\rho V_0^2}$, $Re^* = \frac{Re_g}{Re} = \frac{\rho_g V_g \mu}{\rho V_0 \mu_g}$, and $Ca^* = \frac{Ca_g}{Ca} = \frac{\mu_g V_g}{\mu V_0}$.

Note that the stagnation jet imposes both normal and tangential forces on the droplet surface during the spreading phase. The normal force is induced by the dynamic pressure of the jet, and the ratio of the dynamic pressure of the jet to the droplet is captured by We^* . The jet viscous force produces the shear or tangential force of the jet and Ca^* shows the ratio of jet viscous force to the droplet. For low impact regime, Ca^* is two orders of magnitude greater than We^* , indicating that the jet shear force on the droplet surface is stronger and affects the spreading phase more than the jet normal force. Ebrahim and Ortega³ experimentally observed that the spreading phase was not influenced by the stagnation jet in high to moderate impact regimes, in which both We^* and Ca^* ($Ca^* \leq 0.02$) are negligible. Hence, it could be speculated that for the stagnation jet flow to influence the spreading phase and form a thinner liquid film on the surface, Eq. (37) has to be satisfied.

Correlation for spreading phase under stagnation flow

For $Ca^* < 0.35$, where the stagnation jet does not considerably influence the droplet dynamics, Eq. (31) or (34) is still valid. For $Ca^* \geq 0.35$, the main additional physics is the jet viscous force acting on the droplet surface. As previously discussed, Ca^* captures the ratio of the jet viscous force to the droplet. Hence, the dimensionless time and length [Eqs. (25) and (30)] found for the impact in free-fall were modified to account for the effects of the stagnation jet or Ca^* . The new dimensionless time and length for the impact under the stagnation jet were found empirically by simply adding Ca^* to the group of dimensionless numbers in Eqs. (25) and (30),

$$\hat{\tau} = \tau^* (Ca^*)^{\frac{1}{4}} = \tau \left(\frac{(1 - \cos \theta) Ca^*}{We} \right)^{\frac{1}{4}}, \quad (38)$$

$$\hat{\xi} = \xi^* (Ca^*)^{-\frac{1}{8}} = \xi \left(\frac{1 - \cos \theta}{We Re Ca^*} \right)^{\frac{1}{8}}. \quad (39)$$

The normalized instantaneous droplet diameter under a stagnation jet is shown in Fig. 13 for $Ca^* \geq 0.35$. A curve fit of the data, given as Eq. (40), predicts the instantaneous droplet diameter in the spreading phase accurately up to 15% for $\hat{\tau} \geq 0.15$. This correlation also has higher error for early spreading because of the collapse process that has different physics and scaling. The error is also more severe for the impact under the stagnation jet because the jet flow also affects the collapsing process,

$$\hat{\xi} = 0.90 \hat{\tau}^{0.33} e^{-0.17 \hat{\tau}} \quad (40)$$

for $2.5 \leq We \leq 41.8$, $40 \leq Re \leq 410$, $0.03 \leq We_g \leq 0.2$, and $Ca^* \geq 0.35$.

It is clear in Fig. 13 that the dimensionless time to the maximum spreading diameter under the stagnation jet is $\hat{\tau}_{max} \approx 0.7$. Thus, time to the maximum spreading diameter of a droplet under a stagnation jet can be determined as

$$t_{max} = 0.7 \frac{D_0}{V_0} \left(\frac{We}{(1 - \cos \theta) Ca^*} \right). \quad (41)$$

Consequently, the maximum spreading factor is determined as

$$\xi_{max} = 0.72 \left(\frac{We Re Ca^*}{1 - \cos \theta} \right)^{\frac{1}{8}}. \quad (42)$$

The instantaneous spreading factor for $Ca^* \geq 0.35$ can be computed by substituting Eqs. (38) and (39) into Eq. (40), resulting

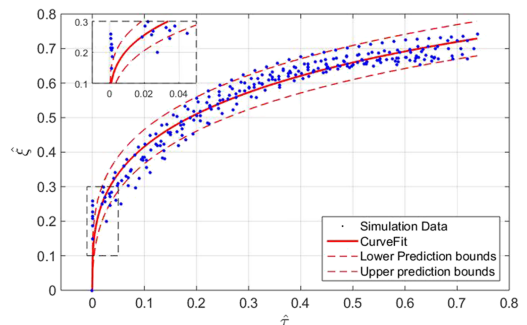


FIG. 13. Normalized instantaneous spreading diameter for droplet impact under stagnation air jet for $Ca^* \geq 0.35$. Simulation data variation: $4.5 \leq We \leq 32$, $135 \leq Re \leq 355$, and $0.032 \leq We_g \leq 0.170$.

in

$$\xi = 0.90\tau^{0.33} \left(\frac{1 - \cos \theta}{We} \right)^{-0.04} Ca^{*0.2} Re^{\frac{1}{8}} \times \exp \left(-0.17\tau \left(\frac{(1 - \cos \theta)Ca^*}{We} \right)^{\frac{1}{4}} \right). \quad (43)$$

The above proposed correlations, Eqs. (43) and (42), can be used to approximate the instantaneous droplet diameter and the maximum spreading factor in a gas-assisted spray cooling regime $10 \leq D \leq 40 \mu\text{m}$ and $10 \leq V_0 \leq 50 \text{ m/s}$, respectively.⁴⁴

CONCLUSIONS

Micrometer droplet impingement was simulated using a 3D lattice Boltzmann method in the low Re and We number regimes. Droplet impact was modeled in ambient air as well as under a stagnation jet air flow to represent the hydrodynamics of single-phase and gas atomized spray cooling, respectively. Numerical data for the impact in ambient air was verified by the experimental data provided by Briones *et al.*¹⁸

The most relevant conclusions can be summarized as follows:

1. We number, Re number, and surface wettability individually affect the hydrodynamics of the impact and therefore these three parameters must be matched in comparing different situations.
2. Micro-scale droplet impingement which leads to low impact We and Re regimes was found to be distinct from the millimeter-sized or moderate to high impact conditions. Most of the analytic models derived for moderate to high impact regimes fail for the low impact regimes.
3. Simulation data for the impact in ambient air and under a stagnation jet were successfully normalized and correlations for the instantaneous droplet spreading phase of both of the cases were proposed. The correlation for the impact in ambient air can be used to approximate the spreading phase in unassisted spray cooling in which the sprayed liquid droplets impact the surface in ambient air. However, the spreading phase in gas-assisted spray cooling, in which the droplets impact the surface while a stagnation jet flow is imposing normal and tangential forces on them, can be approximated using the correlation for the impact under a stagnation jet.
4. Stagnation jet flow was found to influence the hydrodynamics of the spreading regime when the parameter $Ca^* = \frac{\mu_g V_g}{\mu V_0} \geq 0.35$, where $\frac{\mu_g}{\mu}$ is the gas to liquid viscosity ratio, V_g is the jet velocity, and V_0 is the initial droplet impact velocity.

ACKNOWLEDGMENTS

This work was supported by funding from the James R. Birle Endowment to the senior author Dr. Alfonso Ortega.

¹J. Kim, "Spray cooling heat transfer: The state of the art," *Int. J. Heat Fluid Flow* **28**, 753 (2007).

²L. C. Chow, M. S. Sehmbe, and M. R. Pais, "High heat flux spray cooling," *Annu. Rev. Heat Transfer* **8**, 291 (1997).

- ³M. Ebrahim and A. Ortega, "Identification of the impact regimes of a liquid droplet propelled by a gas stream impinging onto a dry surface at moderate to high Weber number," *Exp. Therm. Fluid Sci.* **80**, 168 (2017).
- ⁴A. J. Diaz and A. Ortega, "Gas-assisted droplet impact on a solid surface," *J. Fluids Eng.* **138**, 081104 (2016).
- ⁵C. Stow and M. Hadfield, "An experimental investigation of fluid flow resulting from the impact of a water drop with an unyielding dry surface," *Proc. R. Soc. A* **373**, 419 (1981).
- ⁶C. Mundo, M. Sommerfeld, and C. Tropea, "Droplet-wall collisions: Experimental studies of the deformation and breakup process," *Int. J. Multiphase Flow* **21**, 151 (1995).
- ⁷R. Rioboo, M. Marengo, and C. Tropea, "Time evolution of liquid drop impact onto solid, dry surfaces," *Exp. Fluids* **33**, 112 (2002).
- ⁸S. Sikalo, M. Marengo, C. Tropea, and E. Ganic, "Analysis of impact of droplets on horizontal surfaces," *Exp. Therm. Fluid Sci.* **25**, 503 (2002).
- ⁹S. Sikalo and E. Ganic, "Phenomena of droplet-surface interactions," *Exp. Therm. Fluid Sci.* **31**, 97 (2006).
- ¹⁰L. Xu, W. W. Zhang, and S. R. Nagel, "Drop splashing on a dry smooth surface," *Phys. Rev. Lett.* **94**, 184505 (2005).
- ¹¹J. H. Moon, J. B. Lee, and S. H. Lee, "Dynamic behavior of non-Newtonian droplets impinging on solid surfaces," *Mater. Trans.* **54**, 260 (2013).
- ¹²R. Rioboo, C. Tropea, and M. Marengo, "Outcomes from a drop impact on solid surfaces," *Atomization Sprays* **11**, 155 (2001).
- ¹³A. Yarin, "DROP IMPACT DYNAMICS: Splashing, spreading, receding, bouncing," *Annu. Rev. Fluid Mech.* **38**, 159 (2006).
- ¹⁴R.-H. Chen, L. C. Chow, and J. E. Navedo, "Effects of spray characteristics on critical heat flux in subcooled water spray cooling," *Int. J. Heat Mass Transfer* **45**, 4033 (2002).
- ¹⁵W. Jia and H.-H. Qiu, "Experimental investigation of droplet dynamics and heat transfer in spray cooling," *Exp. Therm. Fluid Sci.* **27**, 829 (2003).
- ¹⁶Y. Son, C. Kim, D. H. Yang, and D. J. Ahn, "Spreading of an inkjet droplet on a solid surface with a controlled contact angle at low Weber and Reynolds numbers," *Langmuir* **24**, 2900 (2008).
- ¹⁷A. J. Diaz and A. Ortega, "Investigation of a gas-propelled liquid droplet impinging onto a heated surface," *Int. J. Heat Mass Transfer* **67**, 1181 (2013).
- ¹⁸A. M. Briones, J. S. Ervin, S. A. Putnam, L. W. Byrd, and L. Gschwender, "Micrometer-sized water droplet impingement dynamics and evaporation on a flat dry surface," *Langmuir* **26**, 13272 (2010).
- ¹⁹X. He and L.-S. Luo, "Theory of the lattice Boltzmann method: From the Boltzmann equation to the lattice Boltzmann equation," *Phys. Rev. E* **56**, 6811 (1997).
- ²⁰A. K. Gunstensen, D. H. Rothman, S. Zaleski, and G. Zanetti, "Lattice Boltzmann model of immiscible fluids," *Phys. Rev. A* **43**, 4320 (1991).
- ²¹M. R. Swift, W. Osborn, and J. Yeomans, "Lattice Boltzmann simulation of nonideal fluids," *Phys. Rev. Lett.* **75**, 830 (1995).
- ²²X. Shan and H. Chen, "Lattice Boltzmann model for simulating flows with multiple phases and components," *Phys. Rev. E* **47**, 1815 (1993).
- ²³X. He, S. Chen, and R. Zhang, "A lattice Boltzmann scheme for incompressible multiphase flow and its application in simulation of Rayleigh-Taylor instability," *J. Comput. Phys.* **152**, 642 (1999).
- ²⁴L. Chen, Q. Kang, Y. Mu, Y.-L. He, and W.-Q. Tao, "A critical review of the pseudopotential multiphase lattice Boltzmann model: Methods and applications," *Int. J. Heat Mass Transfer* **76**, 210 (2014).
- ²⁵X. He, X. Shan, and G. D. Doolen, "Discrete Boltzmann equation model for nonideal gases," *Phys. Rev. E* **57**, R13 (1998).
- ²⁶N. F. Carnahan and K. E. Starling, "Equation of state for nonattracting rigid spheres," *J. Chem. Phys.* **51**, 635 (1969).
- ²⁷A. R. Davies, J. L. Summers, and M. C. T. Wilson, "On a dynamic wetting model for the finite-density multiphase lattice Boltzmann method," *Int. J. Comput. Fluid Dyn.* **20**, 415 (2006).
- ²⁸D. Iwahara, H. Shinto, M. Miyahara, and K. Higashitani, "Liquid drops on homogeneous and chemically heterogeneous surfaces: A two-dimensional lattice Boltzmann study," *Langmuir* **19**, 9086 (2003).
- ²⁹S. Chandra and C. Avedisian, "On the collision of a droplet with a solid surface," *Proc. R. Soc. A* **432**, 13 (1991).
- ³⁰M. Pasandideh Fard, Y. Qiao, S. Chandra, and J. Mostaghimi, "Capillary effects during droplet impact on a solid surface," *Phys. Fluids* **8**, 650 (1996).
- ³¹W.-J. Yang, Report No. 535, Tokyo, University, Institute of Space and Aeronautical Science, 1975, Vol. 40, p. 423.
- ³²H. Jones, "Cooling, freezing and substrate impact of droplets formed by rotary atomization," *J. Phys. D: Appl. Phys.* **4**, 1657 (1971).

- ³³J. Madejski, "Solidification of droplets on a cold surface," *Int. J. Heat Mass Transfer* **19**, 1009 (1976).
- ³⁴P. Attane, F. Girard, and V. Morin, "An energy balance approach of the dynamics of drop impact on a solid surface," *Phys. Fluids* **19**, 012101 (2007).
- ³⁵S. Bechtel, D. Bogy, and F. Talke, "Impact of a liquid drop against a flat surface," *IBM J. Res. Dev.* **25**, 963 (1981).
- ³⁶H.-Y. Kim and J.-H. Chun, "The recoiling of liquid droplets upon collision with solid surfaces," *Phys. Fluids* **13**, 643 (2001).
- ³⁷B. L. Scheller and D. W. Bousfield, "Newtonian drop impact with a solid surface," *AIChE J.* **41**, 1357 (1995).
- ³⁸J. Drelich, E. Chibowski, D. D. Meng, and K. Terpilowski, "Hydrophilic and superhydrophilic surfaces and materials," *Soft Matter* **7**, 9804 (2011).
- ³⁹J. Bico, U. Thiele, and D. Qu, "Wetting of textured surfaces," *Colloids Surf., A* **206**, 41 (2002).
- ⁴⁰D. Nuyttens, K. Baetens, M. De Schampheleire, and B. Sonck, "Effect of nozzle type, size and pressure on spray droplet characteristics," *Biosyst. Eng.* **97**, 333 (2007).
- ⁴¹J. Yang, L. Chow, and M. Pais, "Nucleate boiling heat transfer in spray cooling," *J. Heat Transfer* **118**, 668 (1996).
- ⁴²C. Chang, C.-H. Liu, and C.-A. Lin, "Boundary conditions for lattice Boltzmann simulations with complex geometry flows," *Comput. Math. Appl.* **58**, 940 (2009).
- ⁴³C.-H. Liu, K.-H. Lin, H.-C. Mai, and C.-A. Lin, "Thermal boundary conditions for thermal lattice Boltzmann simulations," *Comput. Math. Appl.* **59**, 2178 (2010).
- ⁴⁴A. Gupta, T. Damm, C. Cook, S. Charagundla, and C. Presser, in *35th Aerospace Science Meeting* (American Institute of Aeronautics and Astronautics, Reno, NV, 1997), Paper No. 97-0268.